PHYSICAL REVIEW B **77**, 094102 (2008)

# Diffuse x-ray scattering from statistically inhomogeneous distributions of threading dislocations beyond the ergodic hypothesis

V. Holý
*Faculty of Mathematics and Physics, Charles University, Prague 11636, Czech Republic*

T. Baumbach, D. Lübbert, L. Helfen, and M. Ellyan
*Institute of Synchrotron Radiation, Forschungszentrum Karlsruhe, Karlsruhe 76133, Germany*

P. Mikulík
*Institute of Condensed Matter Physics, Masaryk University, Brno 60177, Czech Republic*

S. Keller, S. P. DenBaars, and J. Speck
*Department of Electrical and Computer Engineering and Department of Materials, University of California at Santa Barbara, Santa Barbara, California 93106, USA*

(Received 9 December 2007; published 3 March 2008)

Diffuse x-ray scattering from threading dislocations in epitaxial structures is simulated numerically by a Monte Carlo method. The method allows one to simulate diffraction curves for dislocation types, where macroscopic approaches fail. That includes dislocation types for which analytical ensemble averaging is not feasible as well as microdiffraction curves from small sample volumes. In the latter case, the degree of statistic fluctuation of characteristic features is determined. The Monte Carlo method makes it possible to correlate quantitatively the widths of the microdiffraction curves to the densities of various dislocation types. The potential of the method has been demonstrated by a quantitative estimation of the density distribution of edge and screw threading dislocations in laterally overgrown epitaxial GaN structures, which is investigated by a full-field microdiffraction imaging technique. Measuring the asymptotic behavior of the microdiffraction curves allows one to conclude on the prevailing type of threading dislocations.

DOI: 10.1103/PhysRevB.77.094102 PACS number(s): 61.05.cp, 61.72.Dd, 68.55.ag, 81.05.Ea

## I. INTRODUCTION

X-ray diffuse scattering from imperfect crystals is frequently used for the characterization of crystal defects such as clusters of point defects, precipitates of other crystallographic phases, dislocations, or stacking faults. The analysis of the measured data is usually based on the assumption that the diffracted signal is averaged over the statistical ensemble of all possible defect configurations (so-called ergodic hypothesis). If, in addition, the scattering sample is statistically homogeneous (i.e., the defect density is constant in the sample volume), the averaged scattered wave is statistically homogeneous as well, which means that its mutual coherence function (MCF)

$$\Gamma(\mathbf{r},\mathbf{r}') = \langle E(\mathbf{r})E^*(\mathbf{r}')\rangle \qquad (1)$$

is a function of $\mathbf{r}-\mathbf{r}'$ only. In this case, it is suitable to describe the scattered radiation by means of the Fourier transformation $J$ of the MCF, which determines the intensities of the plane components constituting the scattered wave. If the crystal scatters kinematically, this quantity depends only on the scattering vector $\mathbf{Q}=\mathbf{K}-\mathbf{K}_i$, i.e., on the difference of the wave vector of the plane component of the scattered wave and the wave vector $\mathbf{K}_i$ of the incident wave.

Many papers have dealt with the methods of the simulation of $J(\mathbf{Q})$ for various types of defects; these methods are reviewed in Ref. 1. On the other hand, almost no attention has been paid to the case when the ergodic hypothesis is not valid, i.e., when the measured radiation cannot be assumed averaged over the statistical ensemble of all defect configurations. If, for instance, the space resolution in an x-ray imaging method is comparable to the mean distance between the defects, the signal measured by a single detector pixel is not ensemble averaged. This is the case for the imaging of the strain field of individual dislocations,[2] for the microbeam diffraction,[3] or for the full-field microdiffraction imaging from dislocations [often called rocking-curve imaging technique (RCI)]. These methods allow us to *locally* measure the $\mathbf{Q}$ dependence of the scattered intensity, i.e., combining the resolutions in real and reciprocal spaces.

The aim of this paper is to analyze the intensity distribution of the scattered radiation without performing the ensemble averaging, using a recently formulated idea of the calculation of diffuse x-ray scattering from randomly placed dislocations.[4] It will be shown that this approach makes it possible to describe diffuse scattering from the dislocation types, for which the scattering by an individual dislocation can be calculated, but a direct ensemble averaging is not feasible. Further, the method allows for the simulation of microdiffraction data, which is taken at experimental conditions that violate the assumption of ergodicity.

The theoretical method will be used for the determination of the structural quality of epitaxial laterally overgrown (ELO) GaN layers. In these systems, an epitaxial GaN layer grows through windows in an oxide mask deposited onto a GaN buffer layer. The laterally overgrown parts of the structure ("wings") have a better structure quality than the parts of the ELO structure directly above the mask window. In order to determine the structures of the wing and window parts of an ELO structure by x-ray diffraction, it is necessary to distinguish the x-ray signals coming from the wings from those from the windows. Two methods have been used for this purpose. The microbeam diffraction method[3] uses a narrow primary white x-ray beam scanning across the ELO structure; the RCI technique[5] is based on a broad monochromatic parallel primary beam and a two-dimensional detector with the pixel size much smaller than the width of an ELO stripe. The results of both methods indicate that the ELO wings consist of slightly rotated mosaic blocks. The main task in the interpretation of the diffraction widths obtained by both methods mentioned is to distinguish several factors: (i) the mean tilts of the ELO wings, (ii) the tilts of the individual blocks within the wings, (iii) the finite-size effect, and (iv) the diffuse scattering from dislocations in the blocks. This paper concerns the task (iv). In the RCI data, each block gives rise to a bright spot in the space distribution of the diffracted intensity; we measure the angular widths of these local intensity maxima, from which we determine the mean dislocation density inside the blocks and estimate the prevailing type of the dislocations in the blocks.

The paper is organized as follows. In the first part, we review the "conventional" (ensemble-averaged) theory of diffuse scattering based on the Krivoglaz monograph[1] and we apply it for a random set of parallel screw dislocations. In the second part, we present the results of a Monte Carlo simulation of a RCI measurement $I(\mathbf{r};\mathbf{K}_i)$ for a random set of screw and edge threading dislocations perpendicular to the surface. For the former dislocation type, we compare the reciprocal-space widths of the local diffraction maxima with the widths following from the conventional theory. In the third part, we demonstrate the applicability of the theoretical approach in estimating the density of threading dislocations in GaN ELO structures from RCI data.

## II. CONVENTIONAL THEORY OF DIFFUSE SCATTERING

In this section, we derive the expression for an ensemble-averaged Fourier transformation of the MCF. We assume that the sample is statistically homogeneous and we assume the two-beam kinematical approximation and a linearly polarized primary radiation. In contrast to standard formulas in the theory of scattering, we do not restrict ourselves to the far-field limit. We start from the expression for the amplitude of the scattered radiation in point $\mathbf{r}$ outside the crystal,[6]

$$E(\mathbf{r}) = \frac{K^2\chi_{\mathbf{h}}}{4\pi}\int_V d^3\mathbf{r}'\frac{e^{iK|\mathbf{r}-\mathbf{r}'|}}{|\mathbf{r}-\mathbf{r}'|}e^{-i\mathbf{h}\cdot\mathbf{u}(\mathbf{r}')}e^{i\widetilde{\mathbf{K}}_{\mathbf{h}}\cdot\mathbf{r}'}$$
$$\equiv \frac{iK^2\chi_h}{8\pi^2}\int\frac{d^2\mathbf{K}_\parallel}{K_z}e^{i\mathbf{K}\cdot\mathbf{r}}\int_V d^3\mathbf{r}' e^{-i\mathbf{h}\cdot\mathbf{u}(\mathbf{r}')}e^{-i(\mathbf{K}-\widetilde{\mathbf{K}}_{\mathbf{h}})\cdot\mathbf{r}'}. \tag{2}$$

Here, we denoted $K=2\pi/\lambda\equiv|\mathbf{K}|$, $\mathbf{h}$ is the reciprocal-lattice vector (diffraction vector), $\chi_{\mathbf{h}}$ is the $\mathbf{h}$th Fourier component of the crystal polarizability, and $V$ is the sample volume (assumed in the form of a layer with thickness $T$, $x'$, $y'\in(-\infty,\infty)$, $z'\in[-T,0]$). $\mathbf{u}(\mathbf{r}')$ is the random displacement vector in point $\mathbf{r}'$ in the crystal, due to a random set of dislocations. $\mathbf{K}_\parallel$ denotes the component of vector $\mathbf{K}$ parallel to the sample surface, $K_z=\sqrt{K^2-|\mathbf{K}_\parallel|^2}$ is the vertical component of $\mathbf{K}$, and $\widetilde{\mathbf{K}}_{\mathbf{h}}=\mathbf{K}_i+\mathbf{h}$. Figure 1(a) explains the geometrical meaning of vector $\widetilde{\mathbf{K}}_{\mathbf{h}}$.

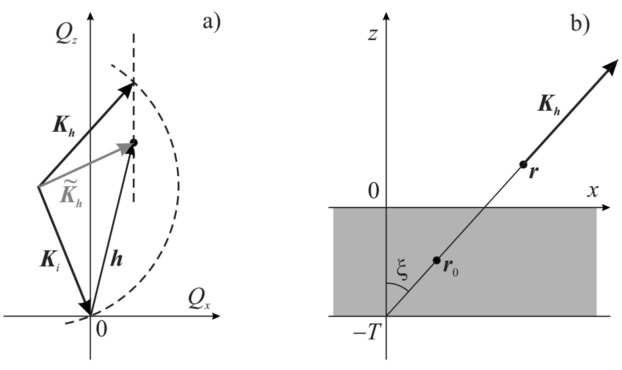

FIG. 1. Sketch of the diffraction geometry (a) in reciprocal space and (b) in real space. The meaning of the symbols is explained in the text.

Substituting the expression for $E(\mathbf{r})$ in Eq. (1) and performing the ensemble averaging, we get an explicit formula for the MCF, which contains the Fourier transformation of the correlation function

$$C(\mathbf{r}''-\mathbf{r}''') = \langle e^{-i\mathbf{h}\cdot[\mathbf{u}(\mathbf{r}'')-\mathbf{u}(\mathbf{r}''')]}\rangle \tag{3}$$

of random displacement field; this function depends only on $\mathbf{r}''-\mathbf{r}'''$ due to the statistical homogeneity of the sample. It can be easily shown that the resulting MCF depends only on $\mathbf{r}-\mathbf{r}'$, i.e., the scattered wave field is statistically homogeneous as well. In Eq. (2) and all following expressions, we assume that the amplitude of the primary radiation is unity.

The intensity $J(\mathbf{K})$ of the plane component of the scattered wave is proportional to the Fourier transformation of the MCF (see Ref. 6) as follows:

$$J(\mathbf{K}) = \frac{K^2K_z^2}{4\pi^2}\int d^2(\mathbf{r}_\parallel-\mathbf{r}'_\parallel)\Gamma(\mathbf{r}-\mathbf{r}')e^{-i\mathbf{K}\cdot(\mathbf{r}-\mathbf{r}')}. \tag{4}$$

Substituting Eq. (2) into Eqs. (1) and (4), we obtain the following after some algebra:

$$J(\mathbf{K}) = \frac{K^6|\chi_{\mathbf{h}}|^2}{32\pi^3}\int d\kappa C^{\mathrm{FT}}(\mathbf{K}_\parallel-\widetilde{\mathbf{K}}_{\mathbf{h}\parallel},\kappa)|S(K_z-\widetilde{K}_{\mathbf{h}z}-\kappa)|^2, \tag{5}$$

where FT denotes the three-dimensional Fourier transformation and

$$S(q) = \int_{-T}^{0} dz e^{-iqz}$$

is the one-dimensional geometrical factor of a layer with thickness $T$. If the crystal is much thicker than the effective defect size (i.e., than the size of the area, where the correlation function $C$ substantially differs from zero), the function

$S$ is much narrower than $C^{\mathrm{FT}}$ and we obtain the well-known formula[1]

$$J(\mathbf{K}) \approx \frac{K^6|\chi_{\mathbf{h}}|^2}{16\pi^2} T C^{\mathrm{FT}}(\mathbf{K}-\widetilde{\mathbf{K}}_{\mathbf{h}}), \tag{6}$$

i.e., the reciprocal-space distribution of diffusely scattered intensity is proportional to the Fourier transformation of the correlation function $C$ of the random displacement field. The intensity $J$ can be expressed as a function of the reduced scattering vector $\mathbf{q}=\mathbf{K}-\widetilde{\mathbf{K}}_{\mathbf{h}}=\mathbf{Q}-\mathbf{h}$.

## III. INTENSITY OF THE DIFFRACTED WAVE BEYOND THE ENSEMBLE AVERAGING

The MCF used in the previous section represents per definition an ensemble-averaged approach. Therefore, in this section, we cannot use Eq. (6) and we start from the expression for the *non averaged amplitude* in Eq. (2). Using a displacement field $\mathbf{u}(\mathbf{r})$ calculated numerically for a set of dislocations, their positions and types being defined using a random-number generator, we obtain the amplitude of the wave scattered from this particular dislocation distribution. However, this "brute-force" calculation is extremely time-consuming due to the numerical calculation of the volume integral $\int_V d^3\mathbf{r}'$ of a very rapidly oscillating function. If we assume that the divergence of the scattered radiation is small, the two-dimensional integral $\int d^2\mathbf{r}_\parallel$ occurring in the left-hand expression in Eq. (2) can be calculated using the stationary phase method[7] and we obtain

$$E(\mathbf{r}) = \frac{K^2\chi_{\mathbf{h}}}{2K_{\mathbf{h}z}} e^{i\mathbf{K}_{\mathbf{h}}\cdot\mathbf{r}} \int_{-T}^{0} dz'\, e^{-i(K_{\mathbf{h}z}-\widetilde{K}_{\mathbf{h}z})z'} e^{-i\mathbf{h}\cdot\mathbf{u}(\mathbf{r}_0)}. \tag{7}$$

Here, we have denoted $\mathbf{K}_{\mathbf{h}}=(\mathbf{K}_{i\parallel}+\mathbf{h}_\parallel, \sqrt{K^2-|\mathbf{K}_{i\parallel}+\mathbf{h}_\parallel|^2})$ the wave vector with the same in-plane component as that of $\widetilde{\mathbf{K}}_{\mathbf{h}}$, but with the length $K$. The vectors $\widetilde{\mathbf{K}}_{\mathbf{h}}$ and $\mathbf{K}_{\mathbf{h}}$ coincide in the diffraction maximum. $\mathbf{r}_0=(x-(z-z')\tan\xi, y, z')$ is the stationary point, $\xi$ is the angle between $\mathbf{K}_{\mathbf{h}}$ and the external surface normal, and the $x$ axis is chosen lying in the sample surface in the scattering plane (see Fig. 1). Equation (7) is better suited for a numerical evaluation; however, we have to examine the validity of the stationary-point approach. In the numerical simulations based on Eq. (7), we set $z=0$, i.e., we assume that the detector plane coincides with the sample surface $z=0$. This simplification has two consequences: (i) In comparison with the intensity measured by a two-dimensional detector perpendicular to the diffracted beam, the simulated intensity distribution is stretched in the $x$ direction by the factor of $1/\cos(\xi)$, and (ii) in the simulation, we completely neglect the influence of the divergence of the diffracted beam on the simulated image. The latter factor smears the measured intensity distribution, but it does not affect the widths of local diffraction curves calculated in the following sections. From a rough numerical estimate, it follows that the smearing of the intensity distribution $I(x,y)$ due to the divergence of the scattered radiation is smaller than 10 $\mu$m for sample-detector distances smaller than 10 cm.

Referring to the previous section, there, obtained results can be reproduced also using the amplitude in Eq. (7) calculated by the stationary-point method. Performing the ensemble averaging, we obtain, similar to Eq. (5), the following:

$$I = \frac{K^4|\chi_{\mathbf{h}}|^2}{32\pi^3 K_{\mathbf{h}z}^2} \int d^3\mathbf{q}\, C^{\mathrm{FT}}(\mathbf{q}) |S(K_{\mathbf{h}z}-\widetilde{K}_{\mathbf{h}z}-q_x\tan\xi-q_z)|^2. \tag{8}$$

This formula can be used for the calculation of the diffraction curve $I(\Delta\alpha_i)$, since the angular deviation $\Delta\alpha_i$ of the primary beam from the diffraction maximum determines the deviation $K_{\mathbf{h}z}-\widetilde{K}_{\mathbf{h}z}$. For a very thick crystal, this intensity has the limiting value

$$I \to \frac{K^4|\chi_{\mathbf{h}}|^2 T}{16\pi^2 K_{\mathbf{h}z}^2} \int d^2\mathbf{q}_\parallel C^{\mathrm{FT}}(\mathbf{q}_\parallel, K_{\mathbf{h}z}-\widetilde{K}_{\mathbf{h}z}-q_x\tan\xi-q_z). \tag{9}$$

Comparing this expression with Eq. (6), we find that the diffraction curve calculated by the stationary-point approach is an integral of the reciprocal-space distribution of the scattered intensity [determined by $C^{\mathrm{FT}}(\mathbf{q})$] over the Ewald sphere, the position of which is determined by the angular deviation $\Delta\alpha_i$. In Fig. 1(a), this Ewald sphere is denoted by the dashed line.

In the next section, we show that, in the case of screw dislocations perpendicular to the sample surface, the correlation function $C(\mathbf{r}-\mathbf{r}')$ does not depend on the vertical coordinates $z$, $z'$. Then, $C^{\mathrm{FT}}(\mathbf{q}) \sim C^{\mathrm{FT}}(\mathbf{q}_\parallel)\delta(q_z)$ and the diffraction curve calculated by the stationary-phase method is

$$I \to \frac{K^4|\chi_{\mathbf{h}}|^2 T}{8\pi K_{\mathbf{h}z}^2} \int dq_y C^{\mathrm{FT}}\left(\frac{(K_{\mathbf{h}z}-\widetilde{K}_{\mathbf{h}z})}{\tan\xi}, q_y\right). \tag{10}$$

Therefore, the intensity calculated by the stationary-point method is the same as the result of the conventional approach integrated over the $q_y$ coordinate perpendicular to the scattering plane.

Summarizing, the stationary-point method and a subsequent ensemble averaging yield comparable results to the conventional approach. If the ensemble averaging cannot be performed, we can use Eq. (7) as an outgoing point for a Monte Carlo simulation, providing the diffracted intensity beyond the application field of the ergodic hypothesis.

## IV. RANDOM SET OF PARALLEL SCREW DISLOCATIONS

We will apply the above approaches for a random set of straight screw dislocations perpendicular to the sample surface. These dislocations occur, for instance, in epitaxial hexagonal GaN(0001) layers[8] (threading dislocations). The total displacement field $\mathbf{u}(\mathbf{r})$ is a superposition of the displacement fields $\mathbf{v}^\alpha(\mathbf{r})$ of individual dislocations

$$\mathbf{u}(\mathbf{r}) = \sum_{\alpha=\uparrow\downarrow} \sum_{\mathbf{R}} \mathbf{v}^\alpha(\mathbf{r}-\mathbf{R}), \tag{11}$$

where $\mathbf{R}$ are the random dislocation positions. The index $\alpha$ denotes the dislocation types; in our model, we assume two types of screw dislocations with the Burgers vectors $\mathbf{b}_{\mathrm{screw}}$

pointing up or down. In the following, we restrict to symmetric diffractions having the diffraction vector $\mathbf{h}$ perpendicular to the surface. Since the displacement field enters all the formulas for the intensity only in the product $\mathbf{h}\cdot\mathbf{u}$, only the vertical component of $\mathbf{v}^{\alpha}$ matters. Theoretical considerations in Refs. 9 and 10 showed that this component is not affected by the surface relaxation of internal stresses, and the formula for the displacement is the same as in an infinite crystal:

$$\mathbf{h}\cdot\mathbf{v}^{\uparrow\downarrow}(\mathbf{r}) = \pm n \arctan(y/x). \tag{12}$$

Here, we have used the fact that the length of the Burgers vector of a screw threading dislocation in a hexagonal GaN is equal to the lattice parameter $c$ and the length of the diffraction vector is $h \equiv h_z = 2\pi n/c$, where $n$ is the diffraction order [we assume the diffraction $(000n)$]. The displacement field does not depend on the vertical coordinate $z$.

In Ref. 11, the diffuse scattering from threading screw dislocations has been dealt with using the conventional theory and explicit formulas have been found for the correlation function. Based on the theoretical approach in Ref. 12, one obtains the following for the symmetric diffraction (0004):

$$C(\mathbf{r}_{\parallel}) = \exp[-T(\mathbf{r}_{\parallel})], \tag{13}$$

$$T(\mathbf{r}_{\parallel}) = \begin{cases} \rho\pi R_c^2 & \text{for } |\mathbf{r}_{\parallel}| > R_c \\ \rho\pi|\mathbf{r}_{\parallel}|^2\left(\dfrac{3|\mathbf{r}_{\parallel}|^2}{R_c^2} - 2 + 8\ln\dfrac{R_c}{|\mathbf{r}_{\parallel}|}\right) & \text{for } |\mathbf{r}_{\parallel}| < R_c, \end{cases}$$

where $\rho$ is the dislocation density and $R_c$ is the so-called cutoff radius, which is usually chosen as $R_c = 1/\sqrt{\rho}$. By deriving Eq. (13), no correlation in the dislocation positions was assumed. Using this expression for $C$ and Eq. (5), we have calculated the reciprocal-space intensity distribution $J(\mathbf{q})$. Since this correlation function $C$ does not depend on $z$, the function $J(\mathbf{q})$ exhibits a narrow streak in reciprocal space parallel to the sample surface. The full width at half maximum (FWHM) of the streak along $q_z$ is inversely proportional to the layer thickness $T$. The intensity integrated over $q_y$

$$\Phi(q_x) = \int dq_y J(\mathbf{q}_{\parallel}, q_z = 0)$$

is shown in Fig. 2. In Fig. 2, only the diffuse part of the scattered intensity is plotted; the coherent part of the diffracted intensity corresponds to the constant asymptotic value of $\lim_{|\mathbf{r}_{\parallel}|\to\infty} C(\mathbf{r}_{\parallel})$. The diffuse part of the scattered intensity is, therefore, proportional to the Fourier transformation of the difference $C(\mathbf{r}_{\parallel}) - \lim_{|\mathbf{r}_{\parallel}|\to\infty} C(\mathbf{r}_{\parallel})$. Since the distribution of the scattered intensity along $q_z$ is very narrow, the function $\Phi(q_x)$ is proportional to the diffraction signal measured by an open detector. In agreement with the theoretical analysis in Ref. 13, the integrated intensity $\Phi(q_x)$ drops asymptotically as $q_x^{-3}$. The FWHM along $q_x$ is proportional to $\sqrt{\rho}$; the shape of the curve sensitively depends on the choice of $R_c$ (see Ref. 11, for details).

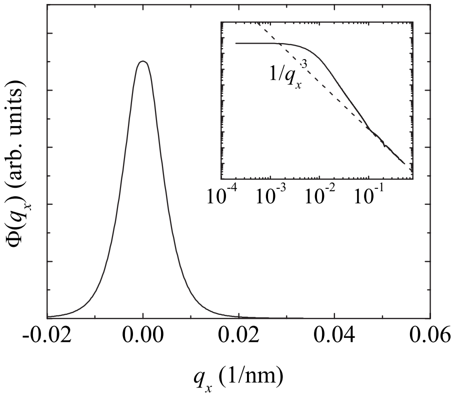

FIG. 2. Integrated reciprocal-space intensity distribution $\Phi(q_x)$ of diffuse scattering from vertical screw dislocations in a (0001)GaN layer, with dislocation density $\rho = 2.5\times10^{7}$ cm$^{-2}$ and symmetric diffraction 0004. In the inset, the asymptotic $q_x^{-3}$ behavior of the intensity is demonstrated.

The simulation of the scattered intensity without performing the ensemble averaging is based on Eq. (7). Figure 3(a) shows the real-space intensity distribution from a single screw dislocation lying in a layer with the thickness $T = 100$ $\mu$m perpendicular to the surface. The intensity was calculated in symmetric 0004 diffraction, with the angular deviation of 0.01° of the primary beam from the diffraction maximum. The $xy$ plane of the picture coincides with the sample surface. The intensity maximum from a single screw dislocation has a horseshoe form. Its end points are the projections of the intersection points of the dislocation line with the upper and lower layer interface in the direction of the diffracted beam. Figure 3(b) shows an intensity distribution calculated for $N = 100$ screw threading dislocations in the square $200\times200$ $\mu$m$^2$ for the angular deviation of 0.01°.

Using a random generator, we have generated a set of screw dislocations with random positions and have randomly chosen two directions of their Burgers vectors ($\mathbf{b}_{\text{screw}}\uparrow\downarrow$). We have assumed that the dislocation positions are com-

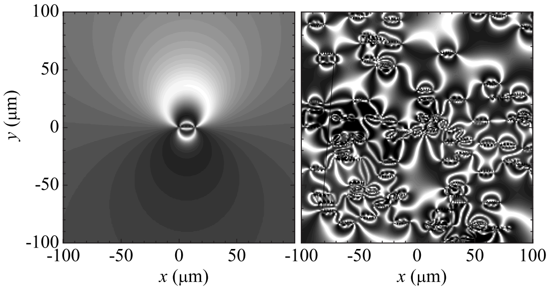

FIG. 3. Real-space distribution of the intensity diffracted from a GaN layer with a single screw dislocation perpendicular to the surface: (left) the dislocation crosses the sample surface in point (0,0) and (right) the intensity distribution from randomly displaced 100 dislocations. Symmetric diffraction 0004, layer thickness $T = 100$ $\mu$m, and angular deviation of the primary wave from the diffraction position was 0.01°. The scattering plane (i.e., the common plane of the primary and scattered wave vectors) is parallel to the $x$ axis.

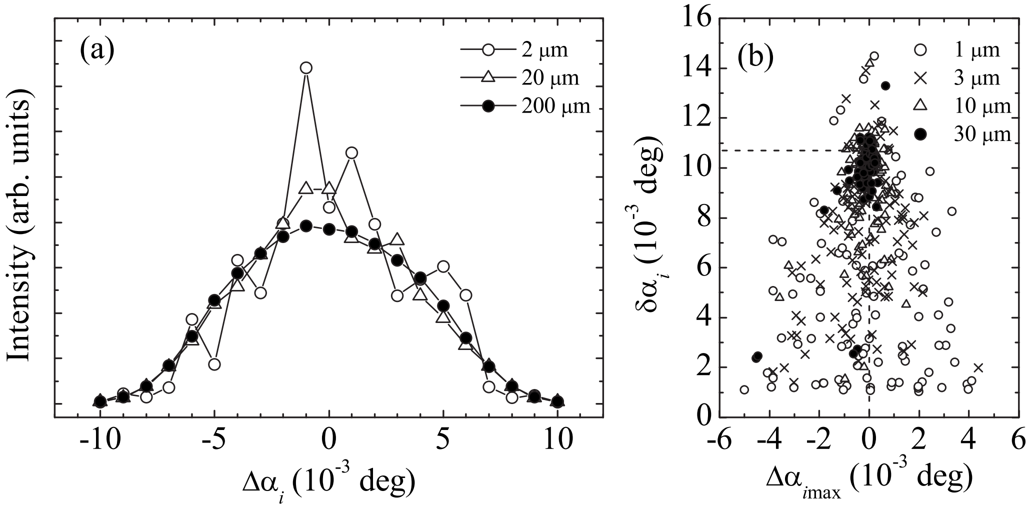

FIG. 4. Local diffraction curves obtained by a Monte Carlo simulation of (a) the diffracted intensity for various sizes $D$ of the integration area and (b) the FWHMs and positions of maxima of the diffraction curves calculated for various $D$'s. The dashed lines in (b) denote the FWHM and maximum position of the ensemble-averaged diffraction curve. In both panels, the size of the definition area was $L=200$ $\mu$m, the dislocation density was $\rho=2.5\times 10^{7}$ cm$^{-2}$, and we used symmetric diffraction 0004.

pletely non correlated and both $\mathbf{b}_{\text{screw}}\uparrow$ and $\mathbf{b}_{\text{screw}}\downarrow$ dislocations have the same density. We have used $N=10^4$ dislocations distributed randomly in a square $(x,y)\in(-L/2,L/2)$, $L=200$ $\mu$m; i.e., the density of both dislocation types together was $\rho=2.5\times 10^{7}$ cm$^{-2}$. Using this random set of dislocations, we have calculated the intensities $I(\mathbf{r};\mathbf{K}_i)$. Then, we have simulated a RCI experiment, calculating the local diffraction curves obtained by numerical integration over a set of randomly placed squares (virtual pixels) with the size $D\leq L$. We have also determined their FWHMs $\delta\alpha_i$ and the relative positions $\Delta\alpha_{i\,\max}$ of their maxima with respect to the diffraction maximum of an ideal layer.

Figure 4(a) shows examples of the local diffraction curves; by increasing $D$, the fluctuations of the resulting intensity decrease. In Fig. 4(b), we have plotted $\delta\alpha_i$ and $\Delta\alpha_{i\,\max}$ for various values of $D$. The value of $\delta\alpha_i$ obtained for $D=L$ is nearly equal to $\delta q_x/h$, where $\delta q_x$ is the FWHM of the intensity distribution $J(q_x)$ calculated by using the conventional approach. Therefore, the value of $L$ chosen is large enough so that the scattered intensity integrated over the entire $L\times L$ area is nearly ensemble averaged. By reducing the integration area $D\times D$, the "intrinsic" fluctuations of the random values $\delta\alpha_i$ and $\Delta\alpha_{i\,\max}$ obtained from various integration areas increase. However, the centroid of the points $(\Delta\alpha_{i\,\max},\delta\alpha_i)$ still well represents the ensemble-averaged values, unless $D$ is comparable to or smaller than the mean distance between the dislocations, $1/\sqrt{\rho}=2$ $\mu$m in our case. If this distance is comparable to or even larger than $D$, some integration areas $D\times D$ contain no dislocations and their diffraction curves are narrower. This is the reason why, for small $D$, the relative amount of integration areas with narrower diffraction curves increases. The distribution of the FWHM values $\delta\alpha_i$ calculated for various pixel sizes $D$ and various dislocation densities $\rho$ follows also from Fig. 5, where we have plotted the numbers of local diffraction curves with the given $\delta\alpha_i$. From Fig. 5, it is obvious that the relative width of the $\delta\alpha_i$ distribution decreases with increasing $D$ and it is almost independent of the dislocation density.

In Fig. 6, we compare the diffraction curve $\Phi(q_x)$ obtained by the ensemble averaging (full line) with the diffraction curve $I(q_x)$ obtained by the Monte Carlo simulation (points); the latter was calculated by the integration of the diffracted intensity over the whole $L\times L$ area. In the latter curve, we used the formula $q_x=h\Delta\alpha_i$, which connects the angular deviation with the position in reciprocal space. This formula holds in a symmetric diffraction only. Obviously, intensity fluctuations are still present; however, the FWHMs of both curves coincide, which can be considered as a proof of the applicability of the stationary-phase method.

## V. RANDOM SET OF EDGE THREADING DISLOCATIONS

It is well known from literature[8] that epitaxial hexagonal GaN(0001) layers, except for the screw threading dislocations, also contain edge threading dislocations with the Bur-

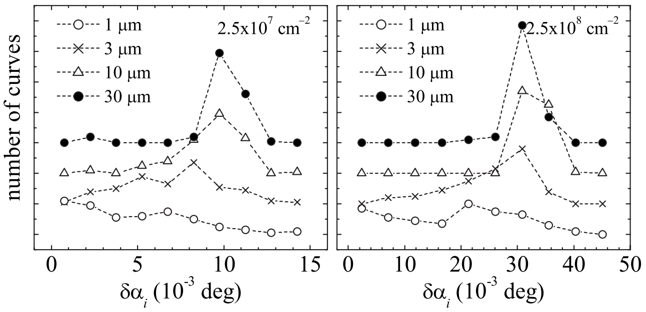

FIG. 5. Relative number of local diffraction curves with a given FWHM $\delta\alpha_i$ calculated for two densities $\rho$ of screw threading dislocations and various pixel sizes $D$. The curves are shifted vertically for clarity.

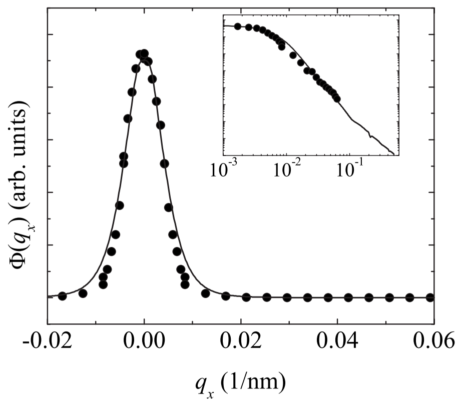

FIG. 6. The ensemble-averaged diffraction curve $\Phi(q_x)$ (full line) and the diffraction curve obtained by the Monte Carlo simulation $I(q_x)$ (points) using $D=L$. All the other parameters are the same as in Fig. 4. The inset shows the diffraction curve in a log-log representation.

gers vectors $\mathbf{b}_{\text{edge}}=\frac{1}{3}\langle 11\bar{2}0\rangle$ parallel to the surface, and mixed dislocations with the Burgers vectors $\mathbf{b}_{\text{mixed}}=\mathbf{b}_{\text{screw}}+\mathbf{b}_{\text{edge}}$. The density of mixed dislocations exceeds the density of the screw threading dislocations by approximately one decade. The displacement field of a mixed dislocation can be expressed as a superposition of pure edge and screw components; in this section, we will investigate only the diffuse scattering from the edge components.

Since, in an infinite medium, the displacement field of a straight edge dislocation is perpendicular to the dislocation line, no diffuse x-ray scattering would occur in an infinite crystal. One can expect that the edge threading dislocations will affect the diffracted intensity in a symmetric diffraction only due to the surface relaxation of internal stresses, which gives rise to a small but nonzero component of the displacement field parallel to the dislocation line,

$$v_z(\mathbf{r}) = \frac{x\nu b_{\text{edge}}}{2\pi(1-\nu)}\frac{z+2r(\nu-1)}{r(r-z)}, \tag{14}$$

where $\nu$ is the Poisson ratio (we neglect the elastic anisotropy) and $x$ is the coordinate parallel to $\mathbf{b}_{\text{edge}}$.[9,10] Diffuse scattering from threading edge dislocations in a symmetrical diffraction is much weaker than the diffuse scattering from screw dislocations, even for a much larger density of the edge threading dislocations.

It is practically impossible to calculate the reciprocal-space distribution $J(\mathbf{q})$ of the scattered intensity for edge threading dislocations using the conventional approach, since such a calculation would be extremely time-consuming. To our knowledge, such a calculation has not been performed yet. In order to assess the contribution of the edge dislocations to the intensity diffracted from an epitaxial GaN layer, we have performed a Monte Carlo simulation analogous to that used for the screw dislocations, for a random set of $10^4$ edge dislocations in the square $L\times L$ ($L=200$ $\mu$m). In the calculation, we have assumed three possible azimuthal directions of $\mathbf{b}_{\text{edge}}$ occurring with the same probability. Figure 7(a) shows the resulting diffraction curve $I(\Delta\alpha_i)$ in the symmetrical 0004 diffraction averaged over the whole square; for the same dislocation density, the curve is approximately three times narrower as that for the screw threading dislocations. In Fig. 7(b), the tails of both diffraction curves are compared. The intensity diffusely scattered from edge threading dislocations drops approximately as $q_x^{-2}$, while for the screw threading dislocation, the intensity decreases roughly as $q_x^{-3}$. This difference in the slopes of the asymptotic parts of the diffraction curves makes it possible to asses the prevailing influence of the screw and edge components of the threading dislocations.

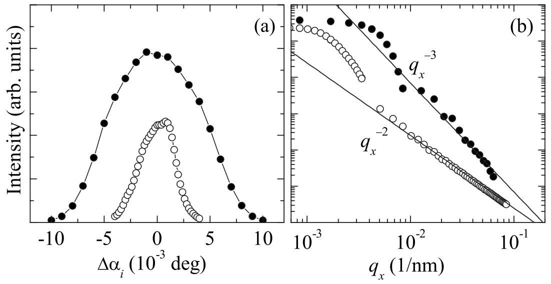

FIG. 7. (a) The diffraction curve of a random set of screw threading dislocations (full points) and edge threading dislocations (empty points) obtained by a Monte Carlo simulation, with $10^4$ dislocations randomly distributed in a square $200\times 200$ $\mu\text{m}^2$. In (b), the tails of the curves are compared.

The FWHMs $\delta\alpha_i$ of the diffraction curves $I(\Delta\alpha_i)$ for screw or edge threading dislocations are proportional to $\sqrt{\rho}$ as follows:

$$\delta\alpha_i = \zeta\sqrt{\rho}.$$

From the conventional method (for the screw dislocations) and from the Monte Carlo simulations (for the edge dislocations), we determined the coefficient $\zeta$ to be $\zeta_{\text{screw}}=2.2\times 10^{-6}$ deg cm and $\zeta_{\text{edge}}=(7.8\pm 0.2)\times 10^{-7}$ deg cm. The latter numerical value was determined from a set of simulations with various microscopic distributions of the edge dislocations.

## VI. EXPERIMENTS

We have used the theory above for the microdiffraction imaging (RCI) of ELO structures on a $c$-plane GaN sample. The sample was grown as follows. First, a GaN seed layer of two 2 $\mu$m thickness has been grown by a standard metal-organic vapor deposition (MOCVD) method. Then, a mask was deposited by a plasma-enhanced chemical vapor deposition of $SiO_2$, followed by a conventional photolithographic patterning. The periodic stripe pattern of 40 $\mu$m periodicity contained stripes of 5 $\mu$m broad windows oriented along the $\langle 1\bar{1}00\rangle$ direction. The lateral overgrowth has been performed by MOCVD at 1270 °C growth temperature in a two step process, changing the $NH_3$ flow $f(NH_3)$ in order to influence the lateral growth velocity [900 s with $f(NH_3)=1$ 1/min and 2700 s with $f(NH_3)=3.6$ 1/min]. We achieved the wing width of 5.9 $\mu$m. The ELO structure is schematically sketched in Fig. 8.

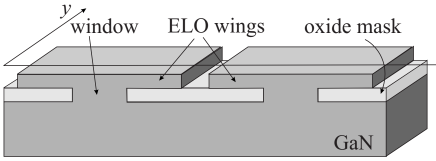

FIG. 8. Sketch of a GaN-ELO structure.

X-ray RCI experiments have been performed at the ID19 beamline for imaging and high resolution diffraction at the ESRF in Grenoble, France. A wide x-ray beam with photon energy of 10.07 keV illuminated a macroscopic part of the sample. The diffracted beam was recorded by a charge coupled device camera with an array of $2048\times2048$ pixels of 1.4 $\mu$m size. By rotating the sample through its 0004 Bragg position, a sequence of digital topographs has been recorded providing simultaneously about $4\times10^6$ local rocking curves, each corresponding to the diffraction profile from an individual microsized sample surface area. The measured intensity $I(x,y,\omega)$ is a function of two coordinates—$x$ (across the ELO stripes) and $y$ (along the ELO stripes) and of the angular position $\omega$ of the sample $(\Delta\omega\equiv\Delta\alpha_i)$.

In Fig. 9, we show an individual rocking curve $I(x=\text{const},y=\text{const},\omega)$ of a single pixel of an ELO wing. The wing volume gives rise to a strong and narrow Bragg peak shifted by its tilt angle with respect to a second lower peak, which stems from the diffraction from the underlying GaN nucleation layer below the oxide mask. In comparison, we show in the same figure the rocking curve averaged over the entire sample surface. Here, we observe the central peak corresponding to both the window region and the nucleation layer, at two side maxima corresponding to the wing areas. The profile of the wing peaks integrated over the sample surface is affected by the tilt variation of the wings and by contributions of possibly several individual grains in the wings (consisting of the local tilt, size broadening, and by diffuse scattering from dislocations). This averaged rocking curve corresponds to the conventional double-crystal rocking curve of this sample region.

The mosaic structure of the ELO pattern follows from Fig. 10, where we have plotted the diffracted intensity $I(x,y=\text{const},\omega)$. Because of the angular tilt of the wing regions with respect to the central window part, the corresponding wing maxima are shifted along the angular $\omega$ axis. In the enlarged part of the $I(x,y=\text{const},\omega)$ intensity distribution (the right panel of Fig. 10), the stripes of the ELO structure are clearly visible.

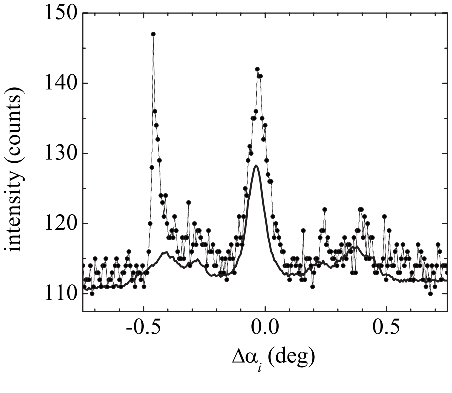

FIG. 9. The rocking curve of an individual pixel of an ELO structure [the pixel position corresponds to the ELO wing (points)] and the rocking curve of the whole sample obtained by the averaging of the rocking curves of individual pixels (full line).

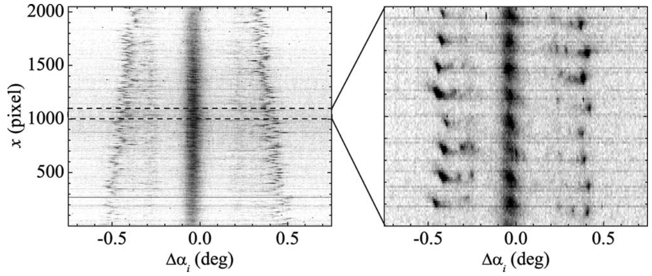

FIG. 10. The intensity distribution $I(x,y=\text{const},\omega)$ measured by the RCI method. One central and four side intensity maxima belong to each ELO stripe. In the enlarged part of the distribution (right panel), the stripes of the ELO structure are clearly visible.

## VII. ANALYSIS OF THE EXPERIMENTAL DATA

In order to conclude on the dislocation density individually from the wings and the window regions in a representative way for the macroscopic sample, we carried out a statistical analysis of the full set of the rocking curves by drawing the two-dimensional histogram of the local rocking-curve width $\delta\alpha_i$ versus their local maximum positions $\Delta\alpha_i$ in Fig. 11. In Fig. 11, the contributions from the window and both wings can be easily separated by its different mean Bragg positions. Further, the contributions of two different main grains within the wings can be identified. Also here, the tilt between the grains, as far as possible, prevents the mixing of influences of small angle grain boundaries and peak distortion due to dislocations on the peak broadening by this procedure.

Let us consider the histogram in Fig. 11 in more detail. The central maximum in Fig. 11 corresponds to the window regions that are not misoriented with respect to the GaN

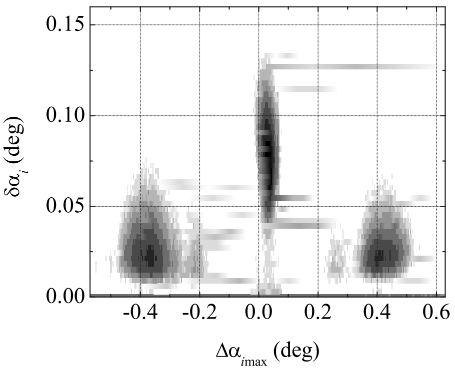

FIG. 11. Two-dimensional histogram of the angular positions $\Delta\alpha_{i\,\max}$ and FWHMs $\delta\alpha_i$ of the local diffraction curves of individual pixels.

nucleation layer ($\Delta\alpha_i=0$). The two maxima on each side of the main peak in Fig. 11 indicate that, in this sample, the ELO wing in a given $y$ position contains, in average, two grains with the misorientations of $\Delta\alpha_i=0.25°$ and $0.36°$, respectively. These two grains correspond to two side maxima on each side of the averaged rocking curve in Fig. 9(b).

The broadening of the central window peak along the abscissa indicates the macroscopic sample curvature in the illuminated area. The additional broadening of the wing peaks can be ascribed to the statistical distribution of the grain tilts, as can be seen in the $I(x=\text{const}, y=\text{const}, \omega)$ intensity map in Fig. 10. The tilt fluctuation is smaller for the grain at smaller tilt angles than at larger tilts. The width of the peaks in the histogram along the ordinate (i.e., along the $\delta\alpha_i$ axis) is mainly caused by fluctuations of the local dislocation density; the influence of the intrinsic FWHM fluctuations as shown in Figs. 4(b) and 5 is at least ten times smaller. However, undisputed, we observe a remarkable difference in the mean half-widths of the wings compared to the window region.

From the averaged FWHMs $\delta\alpha_i$ of the rocking curves (i.e., on the position of the maximum in Fig. 11 on the $\delta\alpha_i$ axis), we can determine the mean dislocation density $\rho$ in the window and wing regions. In the previous section, we have shown that the width of the rocking curve is proportional to $\sqrt{\rho}$. However, the proportionality coefficient $\zeta$ is about three times larger for the screw than for the edge components of the threading dislocations. From the histogram in Fig. 11 alone, it is not possible to distinguish between the two components, but we can determine the upper limits of their densities. In the window region, the maximum possible dislocation densities would be smaller than $\rho_{\text{screw}}^{\text{window}}=1.0\times10^{9}\ \text{cm}^{-2}$ and $\rho_{\text{edge}}^{\text{window}}=1.0\times10^{10}\ \text{cm}^{-2}$, while in the wings, the measurements give evidence of the reduction of the maximum dislocation densities to $\rho_{\text{screw}}^{\text{wing}}=8.1\times10^{7}\ \text{cm}^{-2}$ and $\rho_{\text{edge}}^{\text{wing}}=8.2\times10^{8}\ \text{cm}^{-2}$.

The prevailing dislocation type can be estimated from the asymptotic part of the rocking curve; in the case of screw threadings, the intensity drops as $\Delta\alpha_i^{-3}$, while for edge threadings, it drops as $\Delta\alpha_i^{-2}$. We have averaged the measured local diffraction curves in several $10\times10\ \mu\text{m}^{-2}$ areas. The size of such an area is large enough in order to include a sufficient number of dislocations, but this area contains only one or few individual grains; the diffraction maxima of individual grains can be easily identified. In Fig. 12, we have plotted the outermost tails of several averaged curves from the wing region (i.e., the diffraction curves of single grains in the wing region with the largest tilt). In Fig. 12, the background has been subtracted from the measured intensity and the zero of the $\Delta\alpha_i$ axis has been shifted to the position $\Delta\alpha_{i\,\max}$ of the outermost maximum. From Fig. 12, it follows that, in our sample, the slopes of the diffraction curves are different in different grains and they lie approximately between 2 and 3, so that both screw and edge components of threading dislocations are present in the sample. The available experimental data does not make it possible to determine reliably the densities of individual dislocation types. Since the coefficient $\zeta_{\text{screw}}$ is approximately three times larger than $\zeta_{\text{edge}}$ and the slopes of the intensity tails of various wing regions vary from −2 to −3, we can conclude that in some wing regions, the density of edge threading dislocations can exceed that of screw dislocations by approximately a decade.

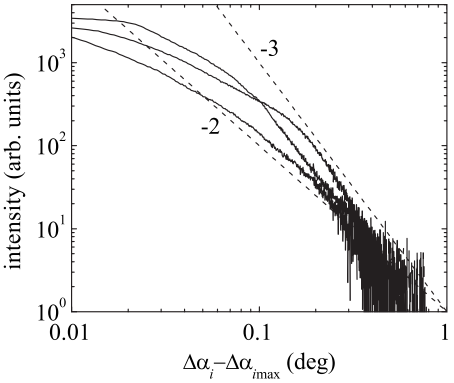

FIG. 12. Diffraction curves of several wing regions in a log-log representation, averaged over $10\times10\ \mu\text{m}^2$ areas.

## VIII. DISCUSSION

In contrast to common x-ray diffractometry, the RCI technique allows us to distinguish the signals coming from individual grains of a mosaic structure. Since the irradiated sample area is very large compared to the grain size, the RCI data allow us to obtain statistically averaged parameters of the mosaic grains. Such a statistical averaging is hard to achieve by means of a scanning microdiffraction, since a successive measurement of many grains by a very narrow primary beam would be very time-consuming and practically impossible.

The RCI technique makes it possible to determine the FWHMs of the rocking curves of individual grains and the positions of the intensity maxima, from which we can determine the averaged FWHM and the corresponding dislocation density *in the grains*, as well as the statistical distribution of the grain tilts. In a conventional x-ray diffractometry technique, the diffracted intensity (not the FWHMs) is averaged over the statistical ensemble so that this value of the FWHM depends mainly on the misorientations of individual grains.

The interpretation of the angular width of a diffraction maximum of a single grain is based on the assumption that its FWHM is caused by the diffuse scattering from dislocations and that it is not affected by the grain form factor (the size-broadening effect). If we denote the FWHM due to the dislocations as $\zeta\sqrt{\rho}$, this assumption is valid if

$$\zeta\sqrt{\rho} \gg \frac{2\pi}{hs} = \frac{c}{ns}, \tag{15}$$

where $h=2\pi n/c$ is the diffraction vector, $s$ is the mean grain size, $c$ is the $c$-lattice parameter, and $n$ is the diffraction order. The mean grain size of the larger, more misoriented grains, which we have taken for our calculations, can be estimated to be larger than $s=4\ \mu\text{m}$ so that the additional broadening of the peaks is less than 10%. Correcting the peak widths to this effect, we obtain the dislocation densities reduced by approximately 20%, i.e., does not affect the order of magnitude of our estimations. In order to analyze this broadening in more detail, a series of measurements with longer diffraction vectors would be necessary, but this was not achievable within our experimental setup.

## IX. CONCLUSION

The paper relates the microscopic and macroscopic theoretical and experimental approaches to x-ray diffraction from randomly distorted single crystals. Therefore, we have developed a theoretical approach describing diffuse x-ray scattering from single crystals containing randomly distributed dislocations without performing the averaging over a statistical ensemble of the dislocation positions. This approach, which is based on a numerical Monte Carlo simulation, allows us to analyze the results of microdiffraction imaging methods, in which the pixel size is smaller or comparable to the mean defect distance. In this case, the data evaluation based on ensemble averaging cannot be simply supposed to be successful to represent the true experimental situation.

By combining the Monte Carlo simulation method with the rocking-curve imaging, we obtain a detailed characterization method of the crystalline perfection in the micrometer scale, which allows us to link the experimental microdiffraction results to the results of conventional x-ray diffractometry.

In the case of laterally structured samples, such as ELO structures it seems to be the only method that allows us to distinguish the influence of the local ELO wing tilts, the grain splitting in the wings, and the dislocations in the grains. Further, a statistical analysis of measured data enables us to independently determine the average misorientation of the grains and their fluctuations, and the estimation of the prevailing dislocation types (screw and edge threading dislocations) and their average densities within the grains.

## ACKNOWLEDGMENTS

Parts of this work are supported by the research programs MSM0021620834 and MSM0021622410 financed by the Ministry of Education of the Czech Republic, and by the Virtual-Institute PINCH-PHOTONICS program.

---

[1] M. A. Krivoglaz, *X-Ray and Neutron Diffraction in Nonideal Crystals* (Springer, Berlin, 1996); R. Barabash, Mater. Sci. Eng., A **309-310** 49 (2001).

[2] I. K. Robinson, Y. Da, T. Spila, and J. E. Greene, J. Phys. D **38**, A7 (2005).

[3] R. Barabas, G. E. Ice, B. C. Larson, G. M. Pharr, K. S. Chung, and W. Yang, Appl. Phys. Lett. **79**, 749 (2001).

[4] V. M. Kaganer (private communication).

[5] D. Lübbert, T. Baumbach, P. Mikulík, P. Pernot, L. Helfen, R. Köhler, T. M. Katona, S. Keller, and S. P. DenBaars, J. Phys. D **38**, A50 (2005).

[6] U. Pietsch, V. Holý, and T. Baumbach, *High-Resolution X-Ray Scattering From Thin Films to Lateral Nanostructures* (Springer-Verlag, Berlin, 2004).

[7] L. V. Azaroff, *X-Ray Diffraction* (Mc-Graw Hill, New York, 1974).

[8] T. Metzger, R. Hoepler, E. Born, O. Ambacher, M. Stutzmann, R. Stoemmer, M. Schuster, H. Goebel, S. Christiansen, M. Albrecht, and H. P. Strunk, Philos. Mag. A **77**, 1013 (1998).

[9] V. L. Indenbom and J. Lothe, *Elastic Strain Fields and Dislocation Mobility* (North-Holland, Amsterdam, 1992).

[10] S. J. Shaibani and P. M. Hazzledine, Philos. Mag. A **44**, 657 (1981).

[11] S. Daniš, V. Holý, Z. Zhong, G. Bauer, and O. Ambacher, Appl. Phys. Lett. **85**, 3065 (2004).

[12] V. M. Kaganer, R. Kohler, M. Schmidbauer, R. Opitz, and B. Jenichen, Phys. Rev. B **55**, 1793 (1997).

[13] V. M. Kaganer, O. Brandt, A. Trampert, and K. H. Ploog, Phys. Rev. B **72**, 045423 (2005).